Journal of Computational and Applied Mathematics 401 (2022) 113778

Contents lists available at ScienceDirect

Journal of Computational and Applied Mathematics

journal homepage: www.elsevier.com/locate/cam

First- and second-order unconditionally stable direct discretization methods for multi-component Cahn–Hilliard system on surfaces

Yibao Li [a], Rui Liu [a], Qing Xia [a], Chenxi He [a], Zhong Li [b,*]

[a] School of Mathematics and Statistics, Xi'an Jiaotong University, Xi'an 710049, China
[b] School of Marxism, Xi'an Jiaotong University, Xi'an 710049, China

ARTICLE INFO

Article history:
Received 27 January 2021
Received in revised form 30 July 2021

Keywords:
Cahn–Hilliard equation
Laplace–Beltrami operator
Triangular surface mesh
Unconditionally energy-stable
Mass conservation

ABSTRACT

This paper proposes a first- and second-order unconditionally stable direct discretization method based on a surface mesh consisting of piecewise triangles and its dual-surface polygonal tessellation for solving the N-component Cahn–Hilliard system. We define the discretizations of the gradient, divergence, and Laplace–Beltrami operators on triangle surfaces. We prove that the proposed schemes, which combine a linearly stabilized splitting scheme, are unconditionally energy-stable. We also prove that our method satisfies the mass conservation. The proposed scheme is solved by the biconjugate gradient stabilized (BiCGSTAB) method, which can be straightforwardly applied to GPU-accelerated biconjugate gradient stabilized implementation by using the Matlab Parallel Computing Toolbox. Several numerical experiments are performed and confirm the accuracy, stability, and efficiency of our proposed algorithm.

1. Introduction

Many physical and chemical phenomena concerning phase separation patterns occurring on static surfaces can be observed [1–10]. For example, microphase separation occurs during the operation of high-energy fuel cells and the electrodeposition of wastewater metal recovery [1–3]. Under the action of an external electric field, the metal ions in the plating solution undergo liquid phase mass transfer, electrochemical reaction, and electrocrystallization processes to deposit metal atoms on the surface of the cathode. The morphogenesis of organisms, especially the generation of skin patterns such as zebra patterns [4,5] and wing patterns [6], is a classical problem. The block copolymer melts can undergo phase ordering or separation when the temperature drops to a critical point [7–10]. The Cahn–Hilliard(CH) equation [11] plays increasingly important roles in various fields about the numerical simulation of multi-component models, such as computer vision [12,13], volume reconstruction [14,15], computational fluid dynamics and materials science [16–22]. A common feature of these models is that the individual physical phases, chemical components, solid grains are described by separate fields. The multi-component CH system on the curved surface has practical significance and research prospects for the modeling of many physical phenomena.

Because of the lack of analytical solution for the multi-component Cahn–Hilliard equation under general conditions, using numerical methods is an effective way to study the dynamics of vector-valued CH equation. Kim et al. [23] developed

* Corresponding author.
E-mail addresses: yibaoli@xjtu.edu.cn (Y. Li), lizhong229@xjtu.edu.cn (Z. Li).
URL: http://gr.xjtu.edu.cn/web/yibaoli (Y. Li).

https://doi.org/10.1016/j.cam.2021.113778
0377-0427/

a second-order accurate fully implicit discretization method of the ternary CH system by using a nonlinear multigrid method. Copetti [24] proposed an explicit finite element approximation scheme and performed robust experiences to study phase separation in a ternary mixture system. Bhattacharyya et al. [25] proposed a semi-implicit Fourier spectral method to study the evolution of microstructure when a disordered ternary alloy is quenched into a ternary miscibility gap. Lee et al. [26] proposed a second-order temporal accuracy discrete scheme to solve a discrete multi-component CH system at the implicit time level, in which computational complexity is only $O(2(N-1)\times 2(N-1))$. Later, Lee et al. [27] presented a practically unconditionally gradient stable conservative numerical method for solving the CH system representing a model in a decoupled way. The proposed method can significantly reduce the CPU time and memory requirements. Steven [28] proposed an efficiency adaptive nonlinear mesh refinement to solve the regularized, strongly anisotropic CH equation and simulate large-scale coarsening of a corrugated surface. In [29], Yang et al. presented a computationally efficient conservative finite difference scheme for solving the N-component Cahn–Hilliard system on curved surfaces. Li et al. [30] extended the two-dimensional compact scheme for the Cahn–Hilliard equation to three-dimensional space, which has second-order accuracy in time and fourth-order accuracy in space. Yang et al. [31,32] developed a two second-order in time, linear and unconditionally energy stable time marching schemes for solving the nonlocal Cahn–Hilliard phase-field model, which is instructive to solve the nonlinear terms implicitly.

Various numerical methods have been developed to solve the partial differential equation on surfaces [33–38]. For example, M.A. Olshanskii and X. Xu [37,38] developed trace finite element method, which uses the restrictions (traces) of a function from the background time-independent finite element space on the reconstructed discrete surface. To the best of our knowledge, there are very few studies which solve the multi-component Cahn–Hilliard system on curved surfaces. Furthermore, the numerical simulation of the multi-component Cahn–Hilliard system takes considerable CPU time for a long time evolution. Therefore, an efficient numerical scheme with good stability on curved surfaces is essential.

In this paper, our main purpose is to develop temporally first- and second-order unconditionally stable direct discretization methods for multi-component Cahn–Hilliard system on surfaces. We performed the discretization via a surface mesh consisting of piecewise triangles and its dual-surface polygonal tessellation. We define the discretizations of the gradient, divergence, and Laplace–Beltrami operators on triangle surfaces. The proposed schemes, which combine a linearly stabilized splitting method, have been proved with the unconditionally energy-stable. To our best knowledge, the schemes developed in this paper are the first provable unconditionally energy stable schemes with second-order accuracy in time for the N-component Cahn–Hilliard system on surfaces. Various numerical tests will be presented to demonstrate the robustness and efficiency of our method.

The remainder of this paper is organized as follows. The multi-component CH system is formulated in Section 2. The implementation of the proposed numerical scheme is described in Section 3. Various numerical simulation results for multi-component CH systems are presented in Section 4. Finally, conclusions are drawn in Section 5.

2. Governing equations

In this Section, we introduce an extended phase field model which is used to deal with multi-component systems. Considering the evolution of the N-component Cahn–Hilliard equation on an arbitrary surface domain $S(\mathbf{s})$. Let us define $\boldsymbol{\phi}(\mathbf{s},\ t)=(\phi_1(\mathbf{s},\ t),\ldots,\phi_N(\mathbf{s},\ t))^T$ as the vector-valued order parameter, where $\phi_i(i=1,\ldots,N)$ is the concentration of one phase, N is the number of phases in multi-component systems (i.e., concentration fraction of different components) and $\mathbf{s}$ lies on the surface S and t is the time. Clearly the sum of different components fractions satisfy

$$\phi_1+\phi_2+\cdots+\phi_N=1. \tag{1}$$

Thus, all of admissible states of different components can be represented as $\{\boldsymbol{\phi}\in\mathbb{R}^N|\sum_{i=1}^N\phi_i=1,\ 0\le\phi_i\le 1\}$. In this model, we use the Ginzburg–Landau free energy to separate the interfaces of N components as:

$$\mathcal{E}(\boldsymbol{\phi}):=\int_S\left(\sum_{i=1}^N F(\phi_i)+\frac{\epsilon^2}{2}\sum_{i=1}^N|\nabla_s\phi_i|^2\right)d\mathbf{x}. \tag{2}$$

Here the free energy $F(\phi_i)$ is defined as $F(\phi_i)=\phi_i^2(1-\phi_i)^2/4$ and ∇_s denotes the surface gradient operator on surface. The evolution of ϕ_i is governed by the H^{-1} gradient of the Ginzburg–Landau energy under Eq. (1) which has to be hold everywhere at any time. The vector-valued CH equation can be derived from the energy functional as follows:

$$\frac{\partial\boldsymbol{\phi}(\mathbf{s},t)}{\partial t}:=\Delta_s\boldsymbol{\mu}(\mathbf{s},t) \tag{3}$$

$$\boldsymbol{\mu}(\mathbf{s},t):=\frac{\delta\mathcal{E}(\mathbf{s},t)}{\delta\boldsymbol{\phi}(\mathbf{s},t)}=F'(\boldsymbol{\phi}(\mathbf{s},t))-\epsilon^2\Delta_s\boldsymbol{\phi}(\mathbf{s},t)+\alpha(\boldsymbol{\phi})\cdot\mathbf{1}, \tag{4}$$

$$\phi_i(\mathbf{s},0)=\phi_i^0(\mathbf{s}),\quad i=1,\ldots,N, \tag{5}$$

$$\nabla_s\phi_i\cdot\mathbf{n}=\nabla_s\mu_i\cdot\mathbf{n}=0,\ \mathbf{s}\in\partial S, \tag{6}$$

where $\mu:=(\mu_1,\ldots,\mu_N)^T$ is the chemical potential which is derived from the variational derivative $\frac{\delta\mathcal{E}}{\delta\boldsymbol{\phi}_i},(i=1,2,\ldots,N)$ of energy $\mathcal{E}$, ϵ is a positive gradient energy coefficient, $\mathbf{1}=(1,\ldots,1)\in\mathbb{R}^N$, $\mathbf{n}$ is the outward unit normal vector to ∂S

and Δ_s is the well-known surface Laplacian–Beltrami operator. To simplify the presentation, here we consider Neumann boundary conditions for both the order parameter and the chemical potential. Note that our method works well under periodic, Neumann, and Dirichlet boundary conditions [33,39,40]. In order to ensure the constraint (1), we use a variable Lagrange multiplier $\alpha(\boldsymbol{\phi})$ here to correct the sum of all components. Based on Eq. (1), we have

$$0 = \frac{\partial(\sum_{i=1}^{N}\phi_i)}{\partial t} = \sum_{i=1}^{N}\frac{\partial \phi_i}{\partial t} = \Delta_s\sum_{i=1}^{N}\mu_i = \Delta_s\Big(\sum_{i=1}^{N}F'(\phi_i) - \epsilon^2\Delta_s\Big(\sum_{i=1}^{N}\phi_i\Big) + N\alpha(\boldsymbol{\phi})\Big), \tag{7}$$

which leads to

$$\alpha(\boldsymbol{\phi}) = -\frac{1}{N}\sum_{i=1}^{N}F'(\phi_i). \tag{8}$$

In the present study, the Lagrangian undetermined multiplier $\alpha(\boldsymbol{\phi})$ used in Eq. (8) is based on the form in Refs. [26,27,41,42] for holding the additional constraint in Eq. (1). The total energy can be deduced to decrease over time as follows:

$$\begin{aligned}\frac{d\mathcal{E}(\mathbf{s},t)}{dt} &= \int_S\sum_{i=1}^{N}(F'(\phi_i(\mathbf{s},t))\frac{\partial\phi_i(\mathbf{s},t)}{\partial t} + \epsilon^2\nabla_s\phi_i(\mathbf{s},t)\cdot\nabla_s\frac{\partial\phi_i(\mathbf{s},t)}{\partial t})d\mathbf{s} \\ &= \int_S\sum_{i=1}^{N}(F'(\phi_i(\mathbf{s},t)) - \epsilon^2\Delta_s\phi_i(\mathbf{s},t))\frac{\partial\phi_i(\mathbf{s},t)}{\partial t}d\mathbf{s} = \int_\Omega\sum_{i=1}^{N}\big(\mu_i(\mathbf{s},t)-\alpha(\phi)\big)\frac{\partial\phi_i(\mathbf{s},t)}{\partial t}d\mathbf{x} \\ &= \int_S\sum_{i=1}^{N}\mu_i(\mathbf{s},t)\Delta_s\mu_i(\mathbf{s},t)d\mathbf{s} - \int_S\alpha(\boldsymbol{\phi})\frac{\partial}{\partial t}\sum_{i=1}^{N}\phi_i(\mathbf{s},t)d\mathbf{s} = -\int_S\sum_{i=1}^{N}|\nabla_s\mu_i(\mathbf{s},t)|^2d\mathbf{s} \le 0.\end{aligned} \tag{9}$$

Here we have used the Neumann boundary conditions for $\boldsymbol{\phi}$ and $\boldsymbol{\mu}$.

3. Numerical method

We now describe the discretizations of the gradient, divergence, and Laplace–Beltrami operators on the triangle surfaces. Let us define a triangle surface mesh as $S = (V, F)$, where $V = \{\mathbf{v}_i | 1 \le i \le N_V\}$ is the vertices set and $F = \{T_k | 1 \le k \le N_F\}$ is the triangles set. N_V and N_F are denoted as the numbers of vertices and triangles on the triangle surface. As shown in Fig. 1, for a given vertex $\mathbf{v} \in V$, we use $I(\mathbf{v})$ to denote the index of 1-ring neighbor of the vertex $\mathbf{v}$ consisting of the 1-ring neighboring vertices $\mathbf{v}_j$ ($j = 0, 1, \ldots, n$ and $\mathbf{v}_0 = \mathbf{v}_n$). The vertices $\mathbf{v}_j$ are labeled counterclockwise. Let T_j be the triangle with vertices $\mathbf{v}$, $\mathbf{v}_j$, and $\mathbf{v}_{j+1}$ and $\mathbf{G}_j$ be the centroid of the triangle T_j, i.e., $\mathbf{G}_j := (\mathbf{v} + \mathbf{v}_j + \mathbf{v}_{j+1})/3$. Furthermore, let $\hat{T}_j$ be the new triangle with vertices $\mathbf{v}$, $\mathbf{G}_j$, $\mathbf{G}_{j+1}$. The normal vector $\mathbf{N}(\mathbf{v})$ can be defined as

$$\mathbf{N}(\mathbf{v}) := \sum_{j=0}^{n-1}\omega_j\mathbf{N}_j / \|\sum_{j=0}^{n-1}\omega_j\mathbf{N}_j\|, \tag{10}$$

where $\mathbf{N}_j$ is the unit normal to triangle T_j at the centroid $\mathbf{G}_j$, i.e., $\mathbf{N}_j := \frac{(\mathbf{v}_j-\mathbf{v})\times(\mathbf{v}_{j+1}-\mathbf{v})}{\|(\mathbf{v}_j-\mathbf{v})\times(\mathbf{v}_{j+1}-\mathbf{v})\|}$. The corresponding centroid weight is $\omega_j := \|\mathbf{G}_j - \mathbf{v}\|^{-2}/\sum_{i=0}^{n-1}\|\mathbf{G}_i - \mathbf{v}\|^{-2}$. The outward normal vectors $\mathbf{n}_{\mathbf{v}_{j+1}}(\mathbf{G}_j)$ and $\mathbf{n}_{\mathbf{v}_{j+1}}(\mathbf{G}_{j+1})$ at the vertices $\mathbf{G}_j$ and $\mathbf{G}_{j+1}$ are defined as [43,44]:

$$\mathbf{n}_{\mathbf{v}_{j+1}}(\mathbf{G}_j) := \frac{(\mathbf{G}_{j+1}-\mathbf{G}_j)\times\mathbf{N}_j}{\|(\mathbf{G}_{j+1}-\mathbf{G}_j)\times\mathbf{N}_j\|} \text{ and } \mathbf{n}_{\mathbf{v}_{j+1}}(\mathbf{G}_{j+1}) := \frac{(\mathbf{G}_{j+1}-\mathbf{G}_j)\times\mathbf{N}_{j+1}}{\|(\mathbf{G}_{j+1}-\mathbf{G}_j)\times\mathbf{N}_{j+1}\|}. \tag{11}$$

Here $\|\cdot\|$ and $\langle\cdot,\cdot\rangle$ denote the normal and inner product of vector, respectively. For a small regular surface $\tilde{\mathcal{S}}$ by using Green's formula, one has

$$\int_{\tilde{\mathcal{S}}}\nabla_d\cdot\mathbf{X}d\mathbf{s} = \int_{\partial\tilde{\mathcal{S}}}\langle\mathbf{X},\ \mathbf{n}\rangle\, d\partial\mathbf{s}. \tag{12}$$

Here, $\mathbf{n}$ is the outer normal vector of the regular surface $\tilde{\mathcal{S}}$. We can obtain

$$\int_{\tilde{\mathcal{S}}}\nabla_s\cdot\mathbf{X}d\mathbf{s} \approx D(\mathbf{v})\nabla_d\cdot\mathbf{X}, \tag{13}$$

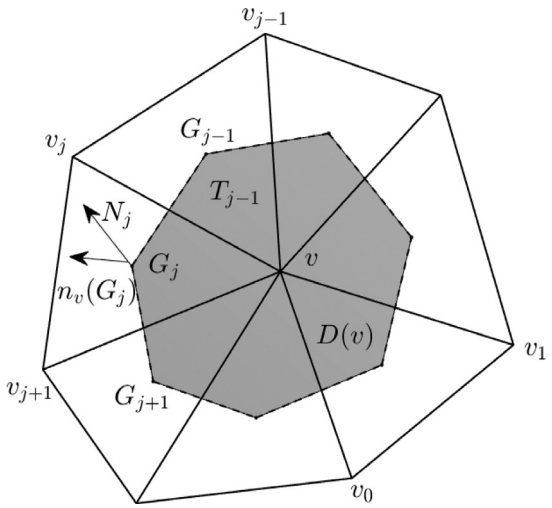

Fig. 1. A vortex $\mathbf{v}$ and its neighbors for evaluating the gradient, divergence, and Laplace–Beltrami operators.

Here $D(\mathbf{v}) := \sum_{j=0}^{n-1} |\hat{T}_j|$ and $|\hat{T}_j|$ is the area of $\hat{T}_j$. $\nabla_d \cdot$ is the discrete divergence operator. On the other hand, it is easy to get

$$\begin{aligned}
&\int_{\partial \bar{S}} \langle \mathbf{X},\ \mathbf{n} \rangle\, d\partial \mathbf{s} \\
&\approx \sum_{j=0}^{n-1} (\|\mathbf{G}_{j+1} - \mathbf{G}_j\|) \int_0^1 \Big\langle q\mathbf{X}(\mathbf{G}_j) + (1-q)\mathbf{X}(\mathbf{G}_{j+1}),\ q\mathbf{n}_{\mathbf{v}_{j+1}}(\mathbf{G}_j) + (1-q)\mathbf{n}_{\mathbf{v}_{j+1}}(\mathbf{G}_{j+1}) \Big\rangle dq \\
&= \sum_{j=0}^{n-1} \frac{\|\mathbf{G}_{j+1} - \mathbf{G}_j\|}{6} \Big(2\left\langle \mathbf{X}(\mathbf{G}_j),\ \mathbf{n}_{\mathbf{v}_{j+1}}(\mathbf{G}_j) \right\rangle + 2\left\langle \mathbf{X}(\mathbf{G}_{j+1}),\ \mathbf{n}_{\mathbf{v}_{j+1}}(\mathbf{G}_{j+1}) \right\rangle \\
&\qquad + \left\langle \mathbf{X}(\mathbf{G}_j),\ \mathbf{n}_{\mathbf{v}_{j+1}}(\mathbf{G}_{j+1}) \right\rangle + \left\langle \mathbf{X}(\mathbf{G}_{j+1}),\ \mathbf{n}_{\mathbf{v}_{j+1}}(\mathbf{G}_j) \right\rangle \Big).
\end{aligned} \tag{14}$$

Here $\mathbf{X}(\mathbf{G}_j) := (\mathbf{X}(\mathbf{v}) + \mathbf{X}(\mathbf{v}_j) + \mathbf{X}(\mathbf{v}_{j+1}))/3$. Eqs. (12)–(14) suggest that we can define the discrete divergence $\nabla_d \cdot \mathbf{X}$ of a vector field $\mathbf{X}$ at $\mathbf{v}$ [33–35,43,44] as

$$\begin{aligned}
\nabla_d \cdot \mathbf{X}(\mathbf{v}) := &\frac{1}{D(\mathbf{v})} \sum_{j=0}^{n-1} \frac{\|\mathbf{G}_{j+1} - \mathbf{G}_j\|}{6} \Big(2\left\langle \mathbf{X}(\mathbf{G}_j),\ \mathbf{n}_{\mathbf{v}_{j+1}}(\mathbf{G}_j) \right\rangle + 2\left\langle \mathbf{X}(\mathbf{G}_{j+1}),\ \mathbf{n}_{\mathbf{v}_{j+1}}(\mathbf{G}_{j+1}) \right\rangle \\
&+ \left\langle \mathbf{X}(\mathbf{G}_j),\ \mathbf{n}_{\mathbf{v}_{j+1}}(\mathbf{G}_{j+1}) \right\rangle + \left\langle \mathbf{X}(\mathbf{G}_{j+1}),\ \mathbf{n}_{\mathbf{v}_{j+1}}(\mathbf{G}_j) \right\rangle \Big).
\end{aligned}$$

We also have the approximating Laplace–Beltrami operator:

$$\begin{aligned}
\Delta_d \phi(\mathbf{v}) := &\frac{1}{D(\mathbf{v})} \sum_{j=0}^{n-1} \frac{\|\mathbf{G}_{j+1} - \mathbf{G}_j\|}{6} \Big(2\left\langle \nabla_d \phi(\mathbf{G}_j),\ \mathbf{n}_{\mathbf{v}_{j+1}}(\mathbf{G}_j) \right\rangle + 2\left\langle \nabla_d \phi(\mathbf{G}_{j+1}),\ \mathbf{n}_{\mathbf{v}_{j+1}}(\mathbf{G}_{j+1}) \right\rangle \\
&+ \left\langle \nabla_d \phi(\mathbf{G}_j),\ \mathbf{n}_{\mathbf{v}_{j+1}}(\mathbf{G}_{j+1}) \right\rangle + \left\langle \nabla_d \phi(\mathbf{G}_{j+1}),\ \mathbf{n}_{\mathbf{v}_{j+1}}(\mathbf{G}_j) \right\rangle \Big).
\end{aligned} \tag{15}$$

The definition of the Laplace–Beltrami operator in Eq. (15), requires the gradient of $\phi(\mathbf{G}_j)$ at the centroid $\mathbf{G}_j$ of each triangle, i.e., $\nabla_d \phi(\mathbf{G}_j)$. We use the Taylor expansion for $\phi(\mathbf{v})$, $\phi(\mathbf{v}_j)$ and $\phi(\mathbf{v}_{j+1})$ to obtain the approximate surface gradient of $\phi(\mathbf{G}_j)$ at the centroid $\mathbf{G}_j$ of each triangle:

$$\begin{cases}
\phi(\mathbf{v}) - \phi(\mathbf{G}_j) = \left\langle \nabla_d \phi(\mathbf{G}_j), \mathbf{v} - \mathbf{G}_j \right\rangle + 0.5 \Delta_d \phi(\mathbf{G}_j) \|\mathbf{v} - \mathbf{G}_j\|^2 + O(\|\mathbf{v} - \mathbf{G}_j\|^2), \\
\phi(\mathbf{v}_j) - \phi(\mathbf{G}_j) = \left\langle \nabla_d \phi(\mathbf{G}_j), \mathbf{v}_j - \mathbf{G}_j \right\rangle + 0.5 \Delta_d \phi(\mathbf{G}_j) \|\mathbf{v}_j - \mathbf{G}_j\|^2 + O(\|\mathbf{v}_j - \mathbf{G}_j\|^2), \\
\phi(\mathbf{v}_{j+1}) - \phi(\mathbf{G}_j) = \left\langle \nabla_d \phi(\mathbf{G}_j), \mathbf{v}_{j+1} - \mathbf{G}_j \right\rangle + 0.5 \Delta_d \phi(\mathbf{G}_j) \|\mathbf{v}_{j+1} - \mathbf{G}_j\|^2 + O(\|\mathbf{v}_{j+1} - \mathbf{G}_j\|^2).
\end{cases} \tag{16}$$

Then, we assume that $\nabla_d \phi(\mathbf{G}_j)$ has the following form:

$$\nabla_d \phi(\mathbf{G}_j) := \alpha_j (\mathbf{v}_j - \mathbf{G}_j) + \beta_j (\mathbf{v}_{j+1} - \mathbf{G}_j). \tag{17}$$

where α_j and β_j are constants. By combining Eqs. (16) and (17), we can further obtain the gradient $\nabla_d\phi(\mathbf{G}_j)$ by calculating the solution α_j and β_j of the following equation

$$\begin{pmatrix} \alpha_j \\ \beta_j \\ \gamma_j \end{pmatrix} = \begin{pmatrix} \langle \mathbf{v}_j - \mathbf{G}_j, \mathbf{v} - \mathbf{G}_j \rangle & \langle \mathbf{v}_{j+1} - \mathbf{G}_j, \mathbf{v} - \mathbf{G}_j \rangle & \|\mathbf{v} - \mathbf{G}_j\|^2 \\ \langle \mathbf{v}_j - \mathbf{G}_j, \mathbf{v}_j - \mathbf{G}_j \rangle & \langle \mathbf{v}_{j+1} - \mathbf{G}_j, \mathbf{v}_j - \mathbf{G}_j \rangle & \|\mathbf{v}_j - \mathbf{G}_j\|^2 \\ \langle \mathbf{v}_j - \mathbf{G}_j, \mathbf{v}_{j+1} - \mathbf{G}_j \rangle & \langle \mathbf{v}_{j+1} - \mathbf{G}_j, \mathbf{v}_{j+1} - \mathbf{G}_j \rangle & \|\mathbf{v}_{j+1} - \mathbf{G}_j\|^2 \end{pmatrix}^{-1} \cdot \begin{pmatrix} \phi(\mathbf{v}) - \phi(\mathbf{G}_j) \\ \phi(\mathbf{v}_j) - \phi(\mathbf{G}_j) \\ \phi(\mathbf{v}_{j+1}) - \phi(\mathbf{G}_j) \end{pmatrix}. \tag{18}$$

Therefore, we can rewrite the Laplace–Beltrami operator $\Delta_d\phi(\mathbf{v})$ at vertex $\mathbf{v}$ as

$$\Delta_d\phi(\mathbf{v}_i) = \mathcal{L}_i \begin{pmatrix} \phi(\mathbf{v}_1) \\ \phi(\mathbf{v}_2) \\ \vdots \\ \phi(\mathbf{v}_{N_V}) \end{pmatrix} \quad \text{and} \quad \begin{pmatrix} \Delta_d\phi(\mathbf{v}_1) \\ \Delta_d\phi(\mathbf{v}_2) \\ \vdots \\ \Delta_d\phi(\mathbf{v}_{N_V}) \end{pmatrix} = \begin{pmatrix} \mathcal{L}_1 \\ \mathcal{L}_2 \\ \vdots \\ \mathcal{L}_{N_V} \end{pmatrix} \begin{pmatrix} \phi(\mathbf{v}_1) \\ \phi(\mathbf{v}_2) \\ \vdots \\ \phi(\mathbf{v}_{N_V}) \end{pmatrix}, \tag{19}$$

where $\mathcal{L}_i$ is a $1 \times N_v$ matrix for $i = 1, 2, \ldots, N_v$, which can be obtained by Eqs. (15)–(18). The Laplace matrix $\mathcal{L}$ of surface S is described as $\mathcal{L} = (\mathcal{L}_1, \mathcal{L}_2, \ldots, \mathcal{L}_{N_V})^T$.

3.1. First-order scheme

In this section, we will present a first-order method in time for the multi-component CH system and prove the unconditional energy stability of this system. To solve Eq. (3), we use the linearly stabilized splitting-type scheme [45–47], in which the linear terms are treated implicitly and the nonlinear term is treated explicitly. Then Eqs. (3) and (4) can be discretized with first-order time accuracy as follows:

$$\frac{\phi_{ij}^{n+1} - \phi_{ij}^n}{\Delta t} = \Delta_d \mu_{ij}^{n+1}, \tag{20}$$

$$\mu_{ij}^{n+1} = F'(\phi_{ij}^n) + \lambda(\phi_{ij}^{n+1} - \phi_{ij}^n) - \epsilon^2 \Delta_d \phi_{ij}^{n+1} + \alpha(\boldsymbol{\phi}_j^n), \tag{21}$$

where

$$\alpha(\boldsymbol{\phi}_j^n) = -\frac{1}{N}\sum_{i=1}^{N}(F'(\phi_{ij}^n) + \lambda(\phi_{ij}^{n+1} - \phi_{ij}^n)). \tag{22}$$

Here ϕ_{ij}^n is an approximation of the concentration of the ith component at time $n\Delta t$ and location $\mathbf{v}_j$, i.e., $\phi_i(\mathbf{v}_j, n\Delta t)$, where $n = 1, 2, \ldots, N_t$, $\Delta t = T/N_t$ is the time-step, T is the final time, and N_t is the total number of time-steps. λ is a positive stabilizing parameter. To solve the linear discrete system (20) and (21) at the implicit time level, we rewrite this system as follows:

$$\begin{pmatrix} \mathcal{I} & \Delta t\mathcal{L} \\ -\lambda\mathcal{I} + \epsilon^2\mathcal{L} & \mathcal{I} \end{pmatrix} \begin{pmatrix} \phi_{i1}^{n+1} \\ \vdots \\ \phi_{iN_V}^{n+1} \\ \mu_{i1}^{n+1} \\ \vdots \\ \mu_{iN_V}^{n+1} \end{pmatrix} = \begin{pmatrix} \phi_{i1}^n \\ \vdots \\ \phi_{iN_V}^n \\ F'(\phi_{i1}^n) - \lambda\phi_{i1}^n + \alpha(\boldsymbol{\phi}_1^n) \\ \vdots \\ F'(\phi_{iN_V}^n) - \lambda\phi_{iN_V}^n + \alpha(\boldsymbol{\phi}_{N_V}^n) \end{pmatrix} \tag{23}$$

Here, $\mathcal{I}$ is the $N_V \times N_V$ identity matrix. We use the biconjugate gradient stabilized method to solve Eq. (23), which can be straightforwardly applied to GPU-accelerated biconjugate gradient stabilized implementation by using the Matlab Parallel Computing Toolbox. Since the residual error converges rather quickly to a tolerance 1e − 8 in few iterations, we do not use the preconditioner for applying BiCGSTAB.

Theorem 3.1. *The solution of the first-order method Eqs. (20) and(21) satisfies* $\sum_{i=1}^{N}\phi_{ij}^{n+1} \equiv 1$, *if the initial condition satisfies* $\sum_{i=1}^{N}\phi_{ij}^0 \equiv 1$.

Proof. By summing of all components of Eqs. (20)–(22) for any $\mathbf{v}_j$, we obtain

$$\begin{bmatrix} \frac{\sum_{i=1}^{N}(\phi_{i1}^{n+1} - \phi_{i1}^n)}{\Delta t} \\ \vdots \\ \frac{\sum_{i=1}^{N}(\phi_{iN_V}^{n+1} - \phi_{iN_V}^n)}{\Delta t} \end{bmatrix} = \begin{bmatrix} \sum_{i=1}^{N}(\Delta_d\mu_{i1}^{n+1}) \\ \vdots \\ \sum_{i=1}^{N}(\Delta_d\mu_{iN_V}^{n+1}) \end{bmatrix} = \begin{bmatrix} \Delta_d\sum_{i=1}^{N}(\mu_{i1}^{n+1}) \\ \vdots \\ \Delta_d\sum_{i=1}^{N}(\mu_{iN_V}^{n+1}) \end{bmatrix} = \begin{bmatrix} \Delta_d(\sum_{i=1}^{N} -\epsilon^2\Delta_d\phi_{i1}^{n+1}) \\ \vdots \\ \Delta_d(\sum_{i=1}^{N} -\epsilon^2\Delta_d\phi_{iN_V}^{n+1}) \end{bmatrix} \tag{24}$$

$$i.e.,\ \left(\mathcal{I}+\epsilon^2\Delta t\Delta_d^2\right)\begin{bmatrix}\sum_{i=1}^N\phi_{i1}^{n+1}\\ \vdots\\ \sum_{i=1}^N\phi_{iN_V}^{n+1}\end{bmatrix}=\begin{bmatrix}\sum_{i=1}^N\phi_{i1}^{n}\\ \vdots\\ \sum_{i=1}^N\phi_{iN_V}^{n}\end{bmatrix}, \tag{25}$$

where $\mathcal{I}$ denotes the identity operator. Here we have used Eq. (22) and telescoping cancellation $\sum_{i=1}^N F'(\phi_{ij}^n)+\lambda(\phi_{ij}^{n+1}-\phi_{ij}^n)+N\alpha(\boldsymbol{\phi}_j^n)=0$ in Eq. (24). According to the Levy–Desplanques theorem, $\mathcal{I}+\epsilon^2\Delta t\Delta_d^2$ is non-singular as a strictly diagonally dominant matrix (or an irreducibly diagonally dominant matrix). According to the recursive property of the formula, Eq. (25) can be written as

$$\left(\mathcal{I}+\epsilon^2\Delta t\Delta_d^2\right)^{n+1}\begin{bmatrix}\sum_{i=1}^N\phi_{i1}^{n+1}\\ \vdots\\ \sum_{i=1}^N\phi_{iN_V}^{n+1}\end{bmatrix}=\begin{bmatrix}\sum_{i=1}^N\phi_{i1}^{0}\\ \vdots\\ \sum_{i=1}^N\phi_{iN_V}^{0}\end{bmatrix}. \tag{26}$$

Then $\sum_{i=1}^N\phi_{ij}^{n+1}\equiv 1$ is a unique solution, because $\left(\mathcal{I}+\epsilon^2\Delta t\Delta_d^2\right)^{n+1}$ is the invertible operator and $\sum_{i=1}^N\phi_{ij}^{0}\equiv 1$. Therefore we can obtain $\sum_{i=1}^N\phi_{ij}^{n}\equiv 1$ for all $n>0$ with the initial condition $\sum_{i=1}^N\phi_{ij}^{0}\equiv 1$. □

Due to Theorem 3.1, Eq. (22) can be simplified as

$$\alpha(\boldsymbol{\phi}_j^n)=-\frac{1}{N}\sum_{i=1}^n F'(\phi_{ij}^n). \tag{27}$$

Theorem 3.2. *The first-order numerical scheme has the total mass conservation property and satisfies* $\sum_{\mathbf{v}_j\in S}\phi_{ij}^{n+1}D(\mathbf{v}_j)=\sum_{\mathbf{v}_j\in S}\phi_{ij}^{n}D(\mathbf{v}_j)$.

Proof. By taking the l_2 inner product of $\sum_{\mathbf{v}_j\in S}\phi_{ij}^{n+1}$ and $\sum_{\mathbf{v}_j\in S}\phi_{ij}^{n}$ with $D(\mathbf{v})$, through the difference operation we can obtain that

$$\begin{aligned}
&\sum_{\mathbf{v}_j\in S}\phi_{ij}^{n+1}D(\mathbf{v}_j)-\sum_{\mathbf{v}_j\in S}\phi_{ij}^{n}D(\mathbf{v}_j)\\
=\ &\Delta t\sum_{\mathbf{v}_j\in S}\Delta_d\mu_{ij}^{n+1}D(\mathbf{v}_j)\\
=\ &\Delta t\sum_{\mathbf{v}_j\in S}\left(\sum_{k=0}^{n-1}\frac{\|\mathbf{G}_{k+1}-\mathbf{G}_k\|}{3}\left(2\left\langle\nabla_d\mu_i^{n+1}(\mathbf{G}_k),\ \mathbf{n}_{\mathbf{v}_{k+1}}(\mathbf{G}_k)\right\rangle+2\left\langle\nabla_d\mu_i^{n+1}(\mathbf{G}_{k+1}),\ \mathbf{n}_{\mathbf{v}_{k+1}}(\mathbf{G}_{k+1})\right\rangle\right.\right.\\
&\qquad\left.\left.+\left\langle\nabla_d\mu_i^{n+1}(\mathbf{G}_k),\ \mathbf{n}_{\mathbf{v}_{k+1}}(\mathbf{G}_{k+1})\right\rangle+\left\langle\nabla_d\mu_i^{n+1}(\mathbf{G}_{k+1}),\ \mathbf{n}_{\mathbf{v}_{k+1}}(\mathbf{G}_k)\right\rangle\right)\right).
\end{aligned}\tag{28}$$

Let $\overline{\mathbf{G}_k\mathbf{G}_{k+1}}$ denote the edge of $\mathbf{G}_k\mathbf{G}_{k+1}$. It is obvious that $\overline{\mathbf{G}_k\mathbf{G}_{k+1}}$ belongs to the dual mesh $D(\mathbf{v}_j)$ with the vertex $\mathbf{v}_j$ and the adjacent neighbor dual mesh $D(\mathbf{v}_{k+1})$ of the vertex $\mathbf{v}_{k+1}$. Therefore, in Eq. (28), we can rewrite this summation in terms of the edges $\bar{S}$ in the dual mesh S_D:

$$\begin{aligned}
&\sum_{\mathbf{v}_j\in S}\phi_{ij}^{n+1}D(\mathbf{v}_j)-\sum_{\mathbf{v}_j\in S}\phi_{ij}^{n}D(\mathbf{v}_j)\\
=\ &\Delta t\sum_{\overline{\mathbf{G}_k\mathbf{G}_{k+1}}\in\bar{S}}\left(\frac{\|\mathbf{G}_{k+1}-\mathbf{G}_k\|}{3}\left(2\left\langle\nabla_d\mu_i^{n+1}(\mathbf{G}_k),\ \mathbf{n}_{\mathbf{v}}(\mathbf{G}_k)\right\rangle+2\left\langle\nabla_d\mu_i^{n+1}(\mathbf{G}_{k+1}),\ \mathbf{n}_{\mathbf{v}}(\mathbf{G}_{k+1})\right\rangle\right.\right.\\
&\qquad+\left\langle\nabla_d\mu_i^{n+1}(\mathbf{G}_k),\ \mathbf{n}_{\mathbf{v}}(\mathbf{G}_{k+1})\right\rangle+\left\langle\nabla_d\mu_i^{n+1}(\mathbf{G}_{k+1}),\ \mathbf{n}_{\mathbf{v}}(\mathbf{G}_k)\right\rangle\\
&\qquad+2\left\langle\nabla_d\mu_i^{n+1}(\mathbf{G}_k),\ \mathbf{n}_{\mathbf{v}_{k+1}}(\mathbf{G}_k)\right\rangle+2\left\langle\nabla_d\mu_i^{n+1}(\mathbf{G}_{k+1}),\ \mathbf{n}_{\mathbf{v}_{k+1}}(\mathbf{G}_{k+1})\right\rangle\\
&\qquad+\left.\left.\left\langle\nabla_d\mu_i^{n+1}(\mathbf{G}_k),\ \mathbf{n}_{\mathbf{v}_{k+1}}(\mathbf{G}_{k+1})\right\rangle+\left\langle\nabla_d\mu_i^{n+1}(\mathbf{G}_{k+1}),\ \mathbf{n}_{\mathbf{v}_{k+1}}(\mathbf{G}_k)\right\rangle\right)\right).
\end{aligned}$$

It should be noted that in Eq. (28), the sum in the last term is for the vertex $\mathbf{v}$. Since all vertices are labeled counterclockwise, we can recalculate $\mathbf{n}_{\mathbf{v}_{k+1}}(\mathbf{G}_k)$ and $\mathbf{n}_{\mathbf{v}_{k+1}}(\mathbf{G}_{k+1})$ as

$$\begin{aligned}\mathbf{n}_{\mathbf{v}_{k+1}}(\mathbf{G}_k) &= \frac{(\mathbf{G}_k - \mathbf{G}_{k+1}) \times \mathbf{N}_k}{\|(\mathbf{G}_k - \mathbf{G}_{k+1}) \times \mathbf{N}_k\|} = -\mathbf{n}_{\mathbf{v}}(\mathbf{G}_k) \quad \text{and} \\ \mathbf{n}_{\mathbf{v}_{k+1}}(\mathbf{G}_{k+1}) &= \frac{(\mathbf{G}_k - \mathbf{G}_{k+1}) \times \mathbf{N}_{k+1}}{\|(\mathbf{G}_k - \mathbf{G}_{k+1}) \times \mathbf{N}_{k+1}\|} = -\mathbf{n}_{\mathbf{v}}(\mathbf{G}_{k+1}).\end{aligned} \tag{29}$$

By substituting Eq. (29) into Eq. (28) yields, we have

$$\sum_{\mathbf{v}_j \in S} \phi_{ij}^{n+1} D(\mathbf{v}_j) - \sum_{\mathbf{v}_j \in S} \phi_{ij}^{n} D(\mathbf{v}_j) = 0,$$

which suggests that the proposed numerical scheme conserves the total mass. □

Let us define the discrete energy as

$$\mathcal{E}(\boldsymbol{\phi}^n) = \sum_{i=1}^{N} \left((F(\phi_i^n), \mathbf{1})_d + \frac{\epsilon^2}{2} \|\nabla_d \phi_i^{n+1}\|_d^2 \right). \tag{30}$$

Here the discrete l_2 inner product at the vertex and centroid of the triangle face can be represented as

$$(\phi_i, \psi_i)_d = \sum_{j=1}^{N_V} \phi_{ij} \psi_{ij} D_j \quad \text{and} \quad (\nabla_d \phi_i, \nabla_d \psi_i)_d = \sum_{j=1}^{N_V} \left[D_j \sum_{k=0}^{n-1} \nabla_d \phi_i(\mathbf{G}_{jk}) \cdot \nabla_d \psi_i(\mathbf{G}_{jk}) \right],$$

where $D_j = D(\mathbf{v}_j)$ for $j = 1, 2, \ldots, N_V$. In this paper, we consider $\phi_i^0 \in [0, 1]$ and restrict our attention to the order parameter ϕ_i which is bounded, i.e. there exists a constant $\mathcal{M}$ (independent of ϕ_i) such that $|\phi_i| \le \mathcal{M}$. However, since the CH equation does not satisfy the maximum principle, it is very difficult to analytically prove that the solution for the CH equation is bounded. Yue et al. [48] noted that the equilibrium solution to the CH equation is in $[-\beta, 1+\beta]$, where β is a small value related to the thickness ϵ. Li and Kim [33] point that the solution of the CH equation is not equal to, but similar to a hyperbolic tangent profile. In the other hand, if the maximum norm of initial condition ϕ_i^0 is bounded by 1, then the solution for the CH equation is bounded based on our numerical experiments. We note that the condition $|\phi_i| \le \mathcal{M}$ can be satisfied by many physically relevant potentials, because changing the double-well potential F allows to find a global bound for $|F''|$ or changing F for $|\phi_i| \ge \mathcal{M}$ may in practice result in $|\phi_i| \le 2\mathcal{M}$. Therefore, we can consider an assumption, i.e., $\max |F''(\phi_i)| = |3\mathcal{M}^2 - 3\mathcal{M} + 0.5| \le \mathcal{Q}$ and $\mathcal{Q}$ is a positive constant.

Theorem 3.3. *If $\lambda \ge \mathcal{Q}/2$, the scheme Eqs. (20)–(22) satisfy*

$$\mathcal{E}(\boldsymbol{\phi}^{n+1}) \le \mathcal{E}(\boldsymbol{\phi}^n) \tag{31}$$

Proof. By taking the l_2 inner product of Eq. (20) with μ_i^{n+1}, we obtain

$$(\phi_i^{n+1} - \phi_i^n, \mu_i^{n+1})_d = \Delta t (\Delta_d \mu_i^{n+1}, \ \mu_i^{n+1})_d = -\Delta t \|\nabla_d \mu_i^{n+1}\|_d^2. \tag{32}$$

By taking the l_2 inner product of Eq. (21) with $\phi_i^{n+1} - \phi_i^n$, we obtain

$$(F'(\phi_i^n), \phi_i^{n+1} - \phi_i^n)_d = (F(\phi_i^{n+1}) - F(\phi_i^n), \mathbf{1})_d - \frac{1}{2} F''(\hat{\psi}_i^n) \|\phi_i^{n+1} - \phi_i^n\|_d^2, \tag{33}$$

$$\lambda(\phi_i^{n+1} - \phi_i^n, \phi_i^{n+1} - \phi_i^n)_d = \lambda \|\phi_i^{n+1} - \phi_i^n\|_d^2, \tag{34}$$

$$\begin{aligned}\epsilon^2(\Delta_d \phi_i^{n+1}, \phi_i^{n+1} - \phi_i^n)_d &= \epsilon^2(\nabla_d \phi_i^{n+1}, \nabla_d \phi_i^{n+1} - \nabla_d \phi_i^n)_d \\ &= \frac{\epsilon^2}{2}(\|\nabla_d \phi_i^{n+1}\|_d^2 + \|\nabla_d \phi_i^{n+1} - \nabla_d \phi_i^n\|_d^2 - \|\nabla_d \phi_i^n\|_d^2),\end{aligned} \tag{35}$$

$$(\alpha(\boldsymbol{\phi}^n), \phi_i^{n+1} - \phi_i^n)_d = \left(-\frac{1}{N} \sum_{i=1}^{N} F'(\phi_i^n), \ \phi_i^{n+1} - \phi_i^n \right)_d, \tag{36}$$

where we have used the Taylor expansion and mean value theorem for definite integrals in Eq. (33) and $\hat{\psi}_i^{\,n} \in [-\mathcal{M},\ \mathcal{M}]$. By combining the above Eqs. (32)–(36), we have

$$\begin{aligned}&\left(F(\phi_i^{n+1}) - F(\phi_i^n), \mathbf{1}\right)_d + \frac{\epsilon^2}{2}\left(\|\nabla_d\phi_i^{n+1}\| - \|\nabla_d\phi_i^n\|\right)\\ &= -\Delta t\|\nabla_d\mu_i^{n+1}\|_d^2 + -\left(\lambda - \frac{1}{2}F''(\hat{\psi}_i^n)\right)\|\phi_i^{n+1} - \phi_i^n\|_d^2 - \frac{\epsilon^2}{2}\|\phi_i^{n+1} - \phi_i^n\|_d^2 - (\alpha(\boldsymbol{\phi}^n), \phi_i^{n+1} - \phi_i^n)_d.\end{aligned}$$

Then we can get

$$\begin{aligned}\mathcal{E}(\boldsymbol{\phi}^{n+1}) - \mathcal{E}(\boldsymbol{\phi}^n) &= \sum_{i=1}^{N}\left(-\Delta t\|\nabla_d\mu_i^{n+1}\|_d^2 - \left(\lambda - \frac{1}{2}F''(\hat{\psi}_i^n)\right)\|\phi_i^{n+1} - \phi_i^n\|_d^2 - \frac{\epsilon^2}{2}\|\phi_j^{n+1} - \phi_j^n\|_d^2\right)\\ &\quad - \alpha(\boldsymbol{\phi}^n)\left(\mathbf{1},\ \sum_{i=1}^{N}\phi_i^{n+1}\right)_d - \alpha(\boldsymbol{\phi}^n)\left(\mathbf{1},\ \sum_{i=1}^{N}\phi_i^n\right)_d\\ &< -\sum_{i=1}^{N}\left(\Delta t\|\nabla_d\mu_i^{n+1}\|_d^2 + \left(\lambda - \frac{1}{2}F''(\mathcal{M})\right)\|\phi_i^{n+1} - \phi_i^n\|_d^2 + \frac{\epsilon^2}{2}\|\phi_j^{n+1} - \phi_j^n\|_d^2\right) \le 0.\end{aligned} \tag{37}$$

The proof is completed. □

3.2. Second-order scheme

In this section, we propose a method for the multi-component CH equation, which can be discretized with second-order time accuracy as follows:

$$\frac{\phi_{ij}^{n+1} - \phi_{ij}^n}{\Delta t} = \Delta_d\mu_{ij}^{n+\frac{1}{2}}, \tag{38}$$

$$\mu_{ij}^{n+\frac{1}{2}} = F'(\tilde{\phi}_{ij}^{n+\frac{1}{2}}) - \lambda\tilde{\phi}_{ij}^{n+\frac{1}{2}} + \lambda\phi_{ij}^{n+\frac{1}{2}} - \epsilon^2\Delta_d\phi_{ij}^{n+\frac{1}{2}} + \alpha(\tilde{\boldsymbol{\phi}}_j^{n+\frac{1}{2}}). \tag{39}$$

where $\tilde{\phi}_{ij}^{n+\frac{1}{2}} = (3\phi_{ij}^n - \phi_{ij}^{n-1})/2$, $\phi_{ij}^{n+\frac{1}{2}} = (\phi_{ij}^{n+1} + \phi_{ij}^n)/2$, and $\alpha(\tilde{\boldsymbol{\phi}}^{n+\frac{1}{2}}) = -\sum_{i=1}^{N}F'(\tilde{\phi}_{ij}^{n+\frac{1}{2}})/N$.

To solve the linear discrete system (38) and (39) at the implicit time level, we can rewrite this system in a similar manner as Eq. (23) and solve it by using the biconjugate gradient stabilized method. The detail descriptions will be omitted here.

Let us define the discrete pseudo energy as

$$\bar{\mathcal{E}}^d(\boldsymbol{\phi}^{n+1}, \boldsymbol{\phi}^n) = \sum_{i=1}^{N}\left(F(\phi_i^{n+1}),\ (\mathbf{1})_d + \frac{\epsilon^2}{2}\|\nabla_d\phi_i^{n+1}\|_d^2 + \frac{2\lambda - F''(\xi_i)}{4}\|\phi_i^{n+1} - \phi_i^n\|_d^2\right). \tag{40}$$

Here, ξ_i are constants which satisfy

$$\left(F'(\tilde{\phi}_i^{n+\frac{1}{2}}),\ \phi_i^{n+1} - \phi_i^n\right)_d = \left(F(\phi_i^{n+1}) - F(\phi_i^n),\ \mathbf{1}\right)_d - \frac{1}{2}F''(\xi_i)(\phi_i^{n+1} - 2\phi_i^n + \phi_i^{n-1}, \phi_i^{n+1} - \phi_i^n)_d.$$

Theorem 3.4. *The second-order numerical scheme satisfies the total mass conservation property and satisfies*

$$\sum_{\mathbf{v}_j\in S}\phi_{ij}^{n+1}D(\mathbf{v}_j) = \sum_{\mathbf{v}_j\in S}\phi_{ij}^nD(\mathbf{v}_j),$$

Proof. For a more detailed verification, please refer to the similar Theorem 3.2. □

Theorem 3.5. *The solution in the second-order method Eqs. (38) and (39) satisfies* $\sum_{i=1}^{N}\phi_{ij}^{n+1} \equiv 1$ *if an initial condition satisfies* $\sum_{i=1}^{N}\phi_{ij}^0 \equiv 1$.

Proof. For a more detailed verification, please refer to the similar Theorem 3.3. □

Theorem 3.6. *If* $\boldsymbol{\phi}^{n+1}$, $\boldsymbol{\phi}^n$, *and* $\boldsymbol{\phi}^{n-1}$ *are the solutions of Eqs. (38) and (39), then under the condition* $\lambda \ge \mathcal{Q}/2$, *the following energy law holds for any time step* Δt:

$$\bar{\mathcal{E}}^d(\boldsymbol{\phi}^{n+1}, \boldsymbol{\phi}^n) \le \bar{\mathcal{E}}^d(\boldsymbol{\phi}^n, \boldsymbol{\phi}^{n-1}). \tag{41}$$

Proof. By taking the l_2 inner product of Eq. (38) with $\mu_i^{n+\frac{1}{2}}$ for any $\mathbf{v}_j$, we obtain

$$(\phi_i^{n+1}-\phi_i^n,\ \mu_i^{n+\frac{1}{2}})_d = \Delta t(\Delta_d\mu_i^{n+\frac{1}{2}},\ \mu_i^{n+\frac{1}{2}})_d = -\Delta t\|\nabla_d\mu_i^{n+\frac{1}{2}}\|_d^2. \tag{42}$$

By taking the l_2 inner product of Eq. (39) with $\phi_i^{n+1}-\phi_i^n$, we obtain

$$(\phi_i^{n+1}-\phi_i^n,\ \mu_i^{n+\frac{1}{2}})_d = \Big(F'(\tilde{\phi}_i^{n+\frac{1}{2}}) - \lambda\tilde{\phi}_i^{n+\frac{1}{2}} + \lambda\phi_i^{n+\frac{1}{2}} - \epsilon^2\Delta_d\phi_i^{n+\frac{1}{2}} + \alpha(\tilde{\boldsymbol{\phi}}^{n+\frac{1}{2}}),\ \phi_i^{n+1}-\phi_i^n\Big). \tag{43}$$

Here, we can obtain

$$\Big(F'(\tilde{\phi}_i^{n+\frac{1}{2}}),\ \phi_i^{n+1}-\phi_i^n\Big)_d = \big(F(\phi_i^{n+1})-F(\phi_i^n),\ \mathbf{1}\big)_d - \frac{1}{2}F''(\xi_i)(\phi_i^{n+1}-2\phi_i^n+\phi_i^{n-1},\phi_i^{n+1}-\phi_i^n)_d, \tag{44}$$

$$\Big(\lambda(\phi_i^{n+\frac{1}{2}}-\tilde{\phi}_i^{n+\frac{1}{2}}),\ \phi_i^{n+1}-\phi_i^n\Big)_d = \frac{\lambda}{2}\left(\|\phi_i^{n+1}-\phi_i^n\|_d^2 + \|\phi_i^{n+1}-2\phi_i^n+\phi_i^{n-1}\|_d^2 - \|\phi_i^n-\phi_i^{n-1}\|_d^2\right), \tag{45}$$

$$\epsilon^2(\Delta_d\phi_i^{n+\frac{1}{2}},\phi_i^{n+1}-\phi_i^n)_d = \frac{\epsilon^2}{2}(\Delta_d\phi_i^{n+1}+\Delta_d\phi_i^n,\phi_i^{n+1}-\phi_i^n)_d = \frac{\epsilon^2}{2}(\|\nabla_d\phi_i^n\|_d^2 - \|\nabla_d\phi_i^{n+1}\|_d^2). \tag{46}$$

By combining Eqs. (40), (42)–(46), we can obtain

$$\begin{aligned}
&\Big((F(\phi_i^{n+1}),\ \mathbf{1})_d + \frac{\epsilon^2}{2}\|\nabla_d\phi_i^{n+1}\|_d^2 + \frac{2\lambda-F''(\xi_i)}{4}\|\phi_j^{n+1}-\phi_j^n\|_d^2\Big)\\
&\quad - \Big((F(\phi_i^n),\ \mathbf{1})_d + \frac{\epsilon^2}{2}\|\nabla_d\phi_i^n\|_d^2 + \frac{2\lambda-F''(\xi_i)}{4}\|\phi_j^n-\phi_j^{n-1}\|_d^2\Big)\\
&= -\Delta t\|\nabla_d\mu_i^{n+\frac{1}{2}}\|_d^2 - \frac{2\lambda-F''(\xi_i)}{4}\|\phi_i^{n+1}-2\phi_i^n+\phi_i^{n-1}\|_d^2 - (\alpha(\tilde{\boldsymbol{\phi}}^{n+\frac{1}{2}}),\phi_j^{n+1}-\phi_j^n)_d.
\end{aligned} \tag{47}$$

Therefore, we have

$$\begin{aligned}
\bar{\mathcal{E}}^d(\boldsymbol{\phi}^{n+1},\boldsymbol{\phi}^n) - \bar{\mathcal{E}}^d(\boldsymbol{\phi}^n,\boldsymbol{\phi}^{n-1}) &= -\sum_{i=1}^N\Big(\Delta t\|\nabla_d\mu_i^{n+\frac{1}{2}}\|_d^2 + \frac{2\lambda-F''(\xi_i)}{4}\|\phi_i^{n+1}-2\phi_i^n+\phi_i^{n-1}\|_d^2\Big)\\
&\quad + \Big(\alpha(\tilde{\boldsymbol{\phi}}^{n+\frac{1}{2}}),\ \sum_{i=1}^N\phi_i^{n+1}\Big)_d - \Big(\alpha(\tilde{\boldsymbol{\phi}}^{n+\frac{1}{2}}),\ \sum_{i=1}^N\phi_i^n\Big)_d\\
&\le -\sum_{i=1}^N\Big(\Delta t\|\nabla_d\mu_i^{n+\frac{1}{2}}\|_d^2 + \frac{2\lambda-F''(\mathcal{M})}{4}\|\phi_i^{n+1}-2\phi_i^n+\phi_i^{n-1}\|_d^2\Big) \le 0. \quad \square
\end{aligned} \tag{48}$$

Hence, the discrete version of the original energy is non-increasing in time. Therefore, our proposed method is unconditionally energy-stable with a suitable stabilizing parameter λ. It should be noted that the stabilizing parameter λ is chosen as $\lambda \ge \mathcal{Q}/2$, which make the energy strictly non-increasing. If $\phi_i^0 \in [0,1]$, then $\max|F''(\phi_i^0)| = 0.5$. Therefore, in practical simulation, $\mathcal{Q}$ and λ may only need to set to $\mathcal{Q}=1$ and $\lambda = 0.5$, because $\Delta t\|\nabla_d\mu_i^{n+\frac{1}{2}}\|_d^2$ may be not smaller in Eqs. (37) and (48). Compared to the fully Crank–Nicolson scheme, our scheme only requires solving an elliptic equation with constant coefficients at each time step, which makes our method easy to implement.

4. Numerical experiments

In this section, we perform various numerical experiments to demonstrate the non-increasing discrete energy, mass conservation, and the stability of our method. Several tests will be performed to show the temporal evolution of multi-component mixture on complex surface and specified domain. Unless otherwise specified, we take $\epsilon = 0.05$. To generate an oriented triangular mesh connecting with the surface points, we employ the triangle mesh generation algorithm [49–53], in which mesh quality can be significantly improved.

4.1. Non-increasing discrete energy and mass conservation

In this section, we simulated the phase separation of a four-component system on a unit sphere surface. The edge of every triangle on the sphere surface is almost the same as $h = 0.05$. We randomly select four components $\phi_a(\mathbf{v}) = \text{rand}(\mathbf{v})$, $\phi_b(\mathbf{v}) = \text{rand}(\mathbf{v})$, $\phi_c(\mathbf{v}) = \text{rand}(\mathbf{v})$, and $\phi_d(\mathbf{v}) = \text{rand}(\mathbf{v})$. Here rand() is a random number between 0 and 1. Note that $\phi_a \ne \phi_b \ne \phi_c \ne \phi_d$. The initial conditions are chosen as

$$\begin{cases}
\phi_1(\mathbf{v},0) = \phi_a(\mathbf{v})/\big(\phi_a(\mathbf{v})+\phi_b(\mathbf{v})+\phi_c(\mathbf{v})+\phi_d(\mathbf{v})\big)\\
\phi_2(\mathbf{v},0) = \phi_b(\mathbf{v})/\big(\phi_a(\mathbf{v})+\phi_b(\mathbf{v})+\phi_c(\mathbf{v})+\phi_d(\mathbf{v})\big)\\
\phi_3(\mathbf{v},0) = \phi_c(\mathbf{v})/\big(\phi_a(\mathbf{v})+\phi_b(\mathbf{v})+\phi_c(\mathbf{v})+\phi_d(\mathbf{v})\big)\\
\phi_4(\mathbf{v},0) = \phi_d(\mathbf{v})/\big(\phi_a(\mathbf{v})+\phi_b(\mathbf{v})+\phi_c(\mathbf{v})+\phi_d(\mathbf{v})\big)
\end{cases} \tag{49}$$

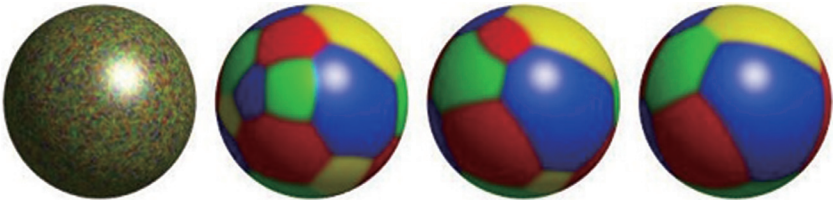

Fig. 2. Evolution of four phases $\boldsymbol{\phi}$ using the second order numerical scheme. From left to right, they are the results at $t = 0,\ 120,\ 240$, and 400. The red, blue, green and yellow regions indicate ϕ_1, ϕ_2, ϕ_3 and ϕ_4, respectively. (For interpretation of the references to color in this figure legend, the reader is referred to the web version of this article.)

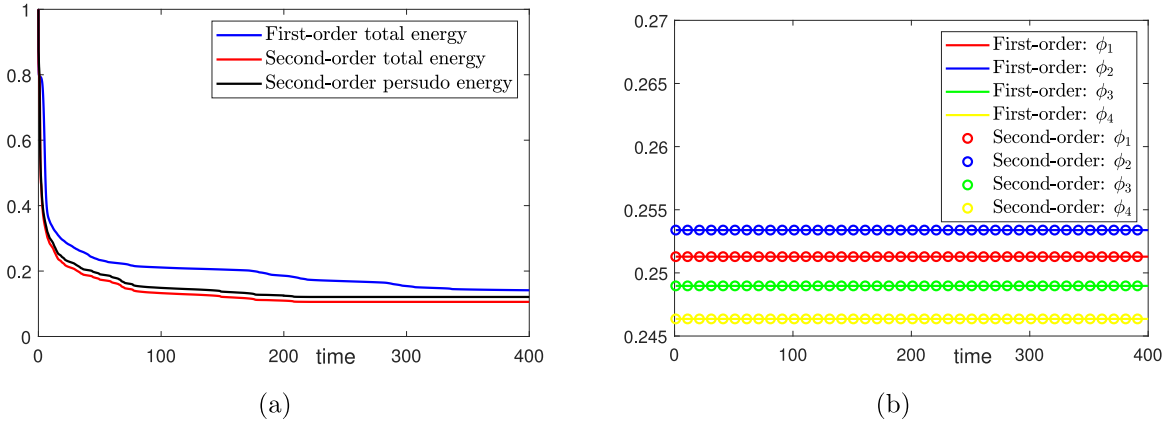

Fig. 3. (a) The non-increasing discrete and pseudo energy for first- and second-order numerical schemes. Here the total energy is normalized by the total energy at the initial time. (b) Mass conservations for first- and second-order numerical schemes.

The calculation is run until $t = 400$ with a time step $\Delta t = 0.1$. Fig. 2 shows the evolution of four phases $\boldsymbol{\phi}$ using the second order numerical scheme. From left to right, they are the results at $t = 0,\ 120,\ 240$, and 400. The red, blue, green and yellow regions indicate ϕ_1, ϕ_2, ϕ_3 and ϕ_4, respectively. Fig. 3(a) and (b) show that the total discrete energy and the pseudo energy of our proposed method are non-increasing with time and mass concentration remains constant, respectively.

4.2. Convergence test

In this section, we perform two numerical experiments to verify the convergence of the first and second order numerical schemes by performing a number of simulations with increasingly finer grids $h = 0.2$, 0.1, 0.05, and 0.025 on the unit sphere surface. The initial conditions are chosen as

$$\begin{cases} \phi_1(x,y,z,0) = 0.25 + 0.25\sin(2\pi x)\sin(2\pi y)\sin(2\pi z) \\ \phi_2(x,y,z,0) = 0.25 + 0.25\cos(2\pi x)\cos(2\pi y)\cos(2\pi z) \\ \phi_3(x,y,z,0) = 0.25 - 0.25\sin(2\pi x)\sin(2\pi y)\sin(2\pi z) \\ \phi_4(x,y,z,0) = 0.25 - 0.25\cos(2\pi x)\cos(2\pi y)\cos(2\pi z) \end{cases} \tag{50}$$

Then the phase separations will be performed with initial conditions of the same mass fraction. Since there is no analytical solution, we assume that the numerical solution generated by the very fine space step $h = 0.005$ and very fine time step $\Delta t = 1 \times 10^{-6}$. We define the error of a grid as the discrete l_2-norm of the difference between that grid and the average of the reference solution cells neighboring it as follows: $e_{h,\ \Delta t_i} := \phi_{h,\ \Delta t_i} - (\zeta_i \phi_p^{\text{ref}} + \eta_i \phi_q^{\text{ref}} + \theta_i \phi_r^{\text{ref}})$. Here, p, q, and r are fine reference grid indexes in a triangle. Furthermore, ζ_i, η_i, and θ_i satisfy $\mathbf{v}_{h,\ \Delta t_i} = \zeta_i \mathbf{v}_p^{\text{ref}} + \eta_i \mathbf{v}_q^{\text{ref}} + \theta_i \mathbf{v}_r^{\text{ref}}$. The rate of convergence is defined as the ratio of successive errors: $\log_2\left(\|e_{h,\ \Delta t}\|_2 / \|e_{\frac{h}{2},\ \frac{\Delta t}{2}}\|_2\right)$. For each grid we integrate over time $T = 1$ with time steps $\Delta t = h^2$ and $\Delta t = 0.1h$ for the first and second order numerical schemes, respectively. The ratio of successive errors can be expected to increase by a factor of 2, i.e., $\|e_{h,\ \Delta t}\|_2 = O(\Delta t + h^2) = O(h^2)$, because $\Delta t = h^2$ and $\Delta t = 0.1h$ are chosen for Eqs. (20)–(21) and Eqs. (38)–(39), respectively. Table 1 shows the convergence rates and l_2 errors of the first- and second-order numerical schemes, respectively. The results suggest that the scheme Eqs. (20)–(21) have second-order accuracy in space and first-order accuracy in time, as expected from the discretization. Furthermore, second-order accuracy with respect to space and time for Eqs. (38)–(39) is observed in Table 1.

Table 1
Convergence rate and error of the proposed schemes. The time steps $\Delta t = h^2$ and $\Delta t = 0.1h$ are chosen for the first and second order numerical schemes, respectively.

h	First-order scheme		Second-order scheme	
	l_2 error	Rate	l_2 error	Rate
0.2	2.984×10^{-3}		1.071×10^{-3}	
0.1	7.395×10^{-4}	2.01	2.556×10^{-4}	2.06
0.05	1.781×10^{-4}	2.05	6.363×10^{-5}	2.00
0.025	4.051×10^{-5}	2.13	1.457×10^{-5}	2.12

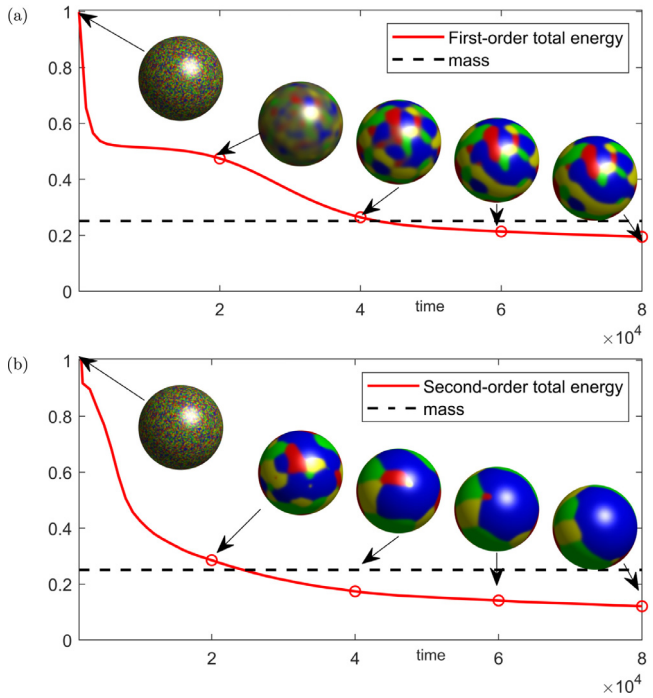

Fig. 4. Stability of (a) first order scheme and (b) second order scheme. The inset subfigures show the morphology of the phase field at the indicated times. Note that we have normalized the total energy by the total energy at the initial time.

4.3. Stability analysis of proposed scheme

The difficulty for an efficient numerical scheme is with the high-order accuracy and strong numerical stability, because the CH equation involves fourth-order spatial derivatives and a nonlinear term. To show the accuracy of the proposed scheme defined in Eqs. (38) and (39), we perform a numerical experiment using a large time step, $\Delta t = 1000$. The initial condition and parameters are set as shown in Section 4.1. The calculations are run until time $T = 80000$ and the numerical solutions are shown in Fig. 4(a) and (b). The two figures show that the mass and total energy evolutions, which suggest that our proposed first- and second-order schemes are indeed unconditionally stable. It is well-known that using a larger time step will cause large error of the numerical solutions. Therefore, a small time step will be used for highly accurate numerical solutions. To maintain our proposed scheme's accuracy and reduce computational costs, an appropriate value for Δt is $\Delta t = 0.2h$.

4.4. Multi-phase separation on unit sphere surface

In this simulation, we consider the multi-phase evolution of two-, three-, four-, and five-component with the same mass fractions on the unit sphere. We use $h = 0.05$ and $\Delta t = 0.01$ on the unit spherical surface. The selection of the initial conditions is similar to Section 4.1. Fig. 5 shows the temporal evolutions of two-, three-, four-, five-component systems, respectively. From the left to right, the times in each row are $t = 0$, 120, 240, and 480, respectively. Each color represents a substance and the phase separation has occurred clearly. As can be seen from these results, our method can effectively simulate multi-component phase separation.

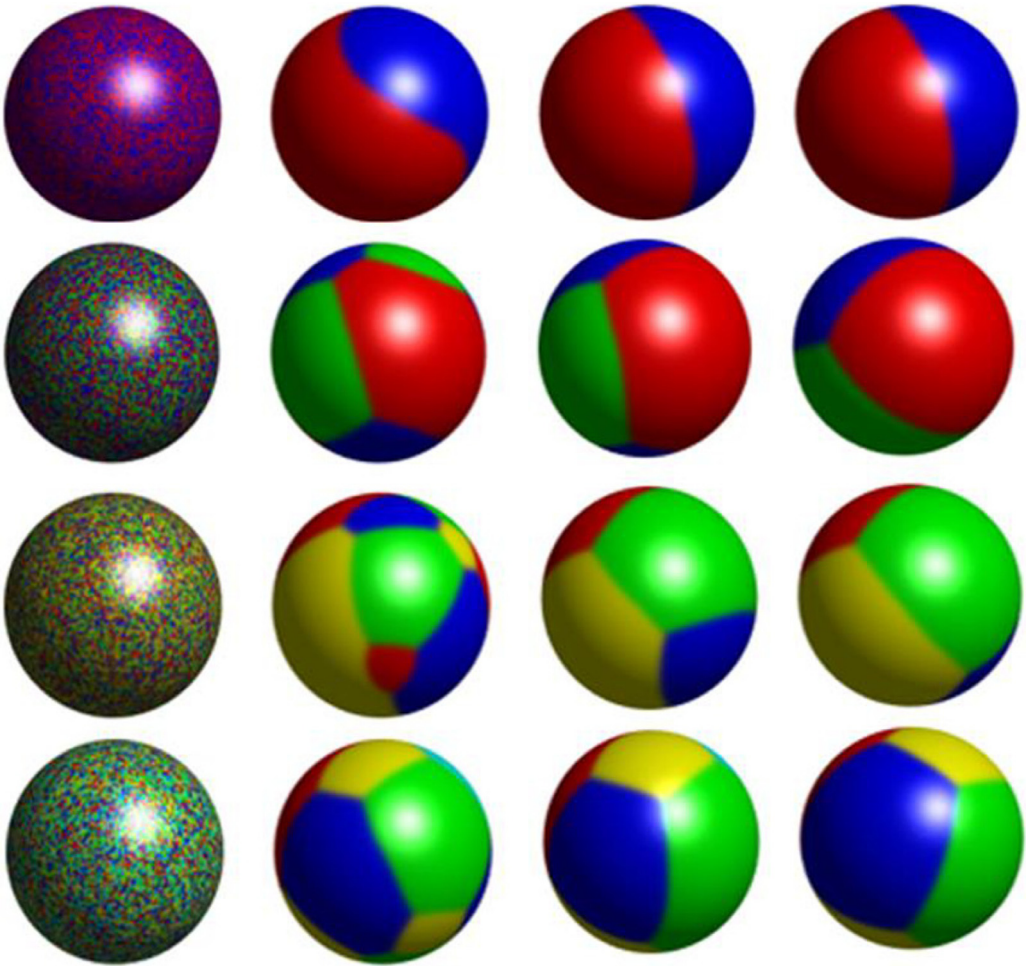

Fig. 5. Time evolution of multi-component separation on sphere surface. From top to bottom, there are the results of evolution for two-, three-, four-, five-component, respectively. From left to right, the computational times are $t = 0, 120, 240$, and 480, respectively. (For interpretation of the references to color in this figure legend, the reader is referred to the web version of this article.)

4.5. Time evolution of multi-phase mixture on complex surface

We consider the numerical simulations of three- and five-component the multi-phase separation on more complex three-dimensional surface such as a bunny surface. Here, we set the initial condition as

$$\begin{cases} \phi_1(\mathbf{v}, 0) = 0.5\cos^4(0.5\text{rand}(\mathbf{v})) \\ \phi_2(\mathbf{v}, 0) = 0.5\sin^4(0.5\text{rand}(\mathbf{v})) \\ \phi_3(\mathbf{v}, 0) = 1 - \phi_1(\mathbf{v}, 0) - \phi_2(\mathbf{v}, 0), \end{cases} \tag{51}$$

and

$$\begin{cases} \phi_1(\mathbf{v}, 0) = 0.5\cos^4(0.5\text{rand}(\mathbf{v})) \\ \phi_2(\mathbf{v}, 0) = 0.5\sin^4(0.5\text{rand}(\mathbf{v})) \\ \phi_3(\mathbf{v}, 0) = 0.4\sin^2(\text{rand}(\mathbf{v})) \\ \phi_4(\mathbf{v}, 0) = 0.5\cos^2(\text{rand}(\mathbf{v})) \\ \phi_5(\mathbf{v}, 0) = 1 - \phi_1(\mathbf{v}, 0) - \phi_2(\mathbf{v}, 0) - \phi_3(\mathbf{v}, 0) - \phi_4(\mathbf{v}, 0), \end{cases} \tag{52}$$

where rand($\mathbf{v}$) is a random number between 0 and 1. Fig. 6(a) and (b) show the phase separation of three-component and five-component mixtures on complex surfaces, respectively. Simulations are run until time $t = 160$ with a time step $\Delta t = 0.01$.

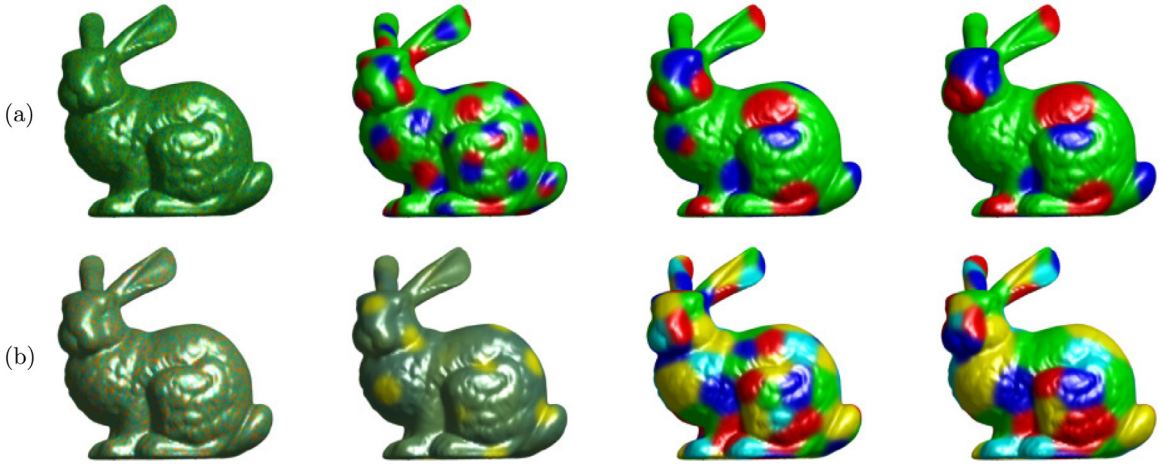

Fig. 6. The temporal evolution of a multi-phase mixture on complex surface with (a) three-component and (b) five-component.

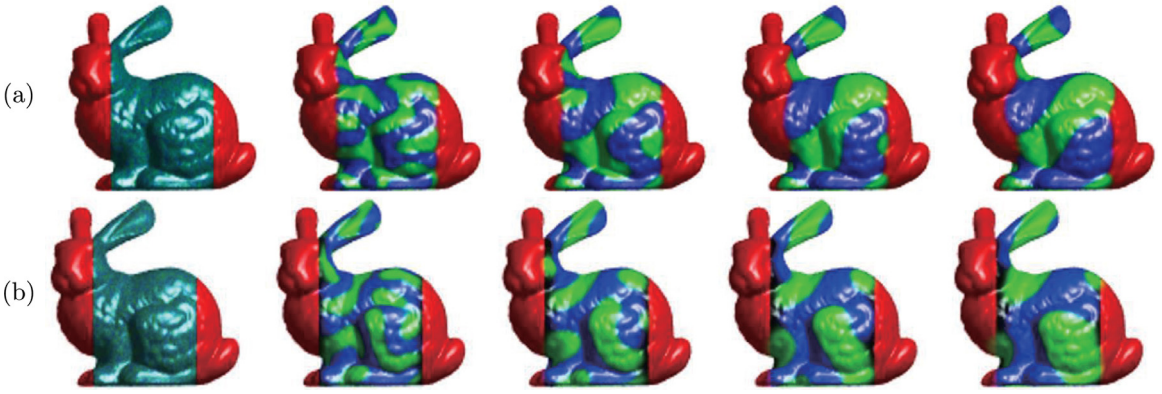

Fig. 7. Time evolution of phase separation in specified domain on bunny surface. From left to right, the computational times are $t = 0$, 5, 25, 50, and 100, respectively. ϕ_1, ϕ_2 and ϕ_3 are represented by the red, blue, and green region, respectively. (a) ϕ_1 is not fixed. (b)ϕ_1 is fixed over time. (For interpretation of the references to color in this figure legend, the reader is referred to the web version of this article.)

4.6. Phase separation in a specified domain on complex surface

In this test, we simulate the binary phase separation in a specified domain on a bunny surface. The initial conditions are chosen as

$$\begin{aligned}
&\phi_1(\mathbf{v}, 0) = \begin{cases} 1 & \text{inside the red region,} \\ 0 & \text{otherwise,} \end{cases} \\
&\phi_2(\mathbf{v}, 0) = [1 - \phi_1(\mathbf{v}, 0)][0.3 + 0.4\text{rand}(\mathbf{v})], \\
&\phi_3(\mathbf{v}, 0) = 1 - \phi_1(\mathbf{v}, 0) - \phi_2(\mathbf{v}, 0).
\end{aligned}$$

Fig. 7 shows the time evolution of phases ϕ_1, ϕ_2, and ϕ_3. Here, ϕ_1, ϕ_2 and ϕ_3 are represented by the red, blue, and green region, respectively. From left to right, the computational times are $t = 0$, 5, 25, 50, and 100, respectively. $\Delta t = 0.01$ is chosen. In Fig. 7(a), we obtain the solutions ϕ_1, ϕ_2 and ϕ_3 by solving Eqs. (38) and (39). While in Fig. 7(b), we fix $\phi_1(\mathbf{v}, t) = \phi_1(\mathbf{v}, 0)$ and obtain the solutions ϕ_2 and ϕ_3 by solving Eqs. (38) and (39). From the results, we can see that if ϕ_1 is fixed over time, the phase separation only occurs inside the specified domain, which is represented by the initial shape of phase ϕ_1. These results imply that our algorithm performs well in specified domain of the complex surface. It should be noted that the phase separation on the fixed surface is only considered in this paper. We can derive the multi-component Cahn–Hilliard system on evolving surfaces by using a conservation law and transport formulae [34] in the future work.

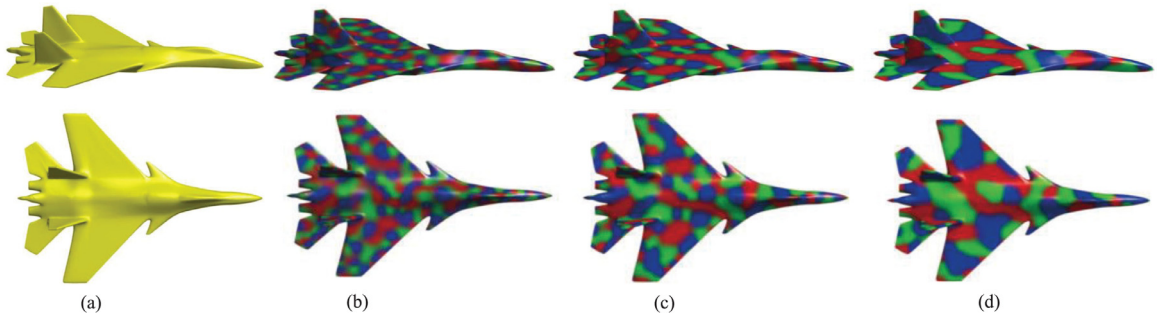

Fig. 8. Evolution of three component Cahn–Hilliard equation on an airplane surface. (a) Airplane surface. (b-d) are the results at time $t = 1$, 5, and 20, respectively. From top to bottom, these are the results in vertical and horizontal views, respectively.

4.7. Multi-component phase separation on real surfaces

To demonstrate the performance of the proposed numerical method, we consider the multi-component phase separation on real surfaces such as airplane. The airplane surface is set in a box $(0, 100)\times(0, 70)\times(0, 25)$ and is discretized by using an unstructured triangular mesh 313943 vertices and 627846 triangles. The following initial condition are chosen $\phi_1(\mathbf{v}, 0) = 0.5\cos^4(0.5\text{rand}(\mathbf{v}))$, $\phi_2(\mathbf{v}, 0) = 0.5\sin^4(0.5\text{rand}(\mathbf{v}))$, and $\phi_3(\mathbf{v}, 0) = 1-\phi_1(\mathbf{v}, 0)-\phi_2(\mathbf{v}, 0)$. The simulation is run up to time $t = 20$ with $\Delta t = 0.01$. Fig. 8(a) shows the airplane surface. Fig. 8(b-d) shows the results of three component phase separation on the airplane surface at time $t = 1$, 5, and 20, respectively. The first and second row show the results in vertical and horizontal views, respectively. These results confirm that the proposed algorithm performs well and results in high visual quality on the complex real surface.

5. Conclusion

In this paper, we propose temporally first- and second-order unconditionally stable direct discretization methods for multi-component Cahn–Hilliard system on surfaces. Discretization is performed via a surface mesh consisting of piecewise triangles and its dual-surface polygonal tessellation. The proposed scheme, which uses linearly stabilized splitting schemes, has been proved with the unconditionally energy stable. The resulting system of discrete equations is solved using a biconjugate gradient stabilized method. We performed several numerical experiments, testing the non-increasing property of discrete energy and mass conservation, the stability of the proposed scheme, time and space convergence, spinodal decomposition with multi-component on different complex surfaces, spinodal decomposition in the specified domain. The numerical experiments demonstrated that our proposed algorithm is fast and efficient.

Acknowledgments

This work was supported by the Fundamental Research Funds for the Central Universities, China (No. XTR042019005) and the China Postdoctoral Science Foundation (No. 2018M640968). The authors thank the reviewers for the constructive and helpful comments on the revision of this article.

References

[1] B. Bozzini, V. Romanello, G.P.D. Gaudenzi, C. Mele, Controlled corrosion of micrometric and submicrometric metal powders in fluidised bed reactor, Trans. IMF 84 (3) (2006) 154–158.
[2] C. Chen, J. Jorn, Fractal analysis of zinc electrodeposition, J. Electrochem. Soc. 137 (7) (1990) 2047–2051.
[3] S. Lucas, P. Moskovkin, Simulation at high temperature of atomic deposition, islands coalescence, Ostwald and inverse Ostwald ripening with a general simple kinetic Monte Carlo code, Thin Solid Films 518 (18) (2010) 5355–5361.
[4] C.P. Gravan, R. Lahoz-Beltra, Evolving morphogenetic fields in the zebra skin pattern based on Turing's morphogen hypothesis, Int. J. Appl. Math. Comput. Sci. 14 (2004) 351–362.
[5] D. Jeong, Y. Li, Y. Choi, M. Yoo, D. Kang, J. Park, J. Choi, J. Kim, Numerical simulation of the zebra pattern formation on a three-dimensional model, Phys. A 475 (2017) 106–116.
[6] S. Liaw, C. Yang, R. Liu, J. Hong, Turing model for the patterns of lady beetles, Phys. Rev. E 64 (4) (2001) 041909.
[7] D. Jeong, J. Kim, Microphase separation patterns in diblock copolymers on curved surfaces using a nonlocal Cahn–Hilliard equation, Eur. Phys. J. E 38 (11) (2015) 117.
[8] F. Liu, N. Goldenfeld, Dynamics of phase separation in block copolymer melts, Phys. Rev. A 39 (9) (1989) 4805.
[9] T. Baumgart, S.T. Hess, W.W. Webb, Imaging coexisting fluid domains in biomembrane models coupling curvature and line tension, Nature 425 (6960) (2003) 821–824.
[10] A.R. Bausch, M.J. Bowick, A. Cacciuto, A.D. Dinsmore, M.F. Hsu, D.R. Nelson, M.G. Nikolaides, A. Travesset, D.A. Weitz, Grain boundary scars and spherical crystallography, Science 299 (5613) (2003) 1716–1718.
[11] J.W. Cahn, J.E. Hilliard, Free energy of a non-uniform system I. Interfacial free energy, J. Chem. Phys. 28 (1958) 258–267.

[12] A. Bertozzi, S. Esedoglu, A. Gillette, Inpainting of binary images using the Cahn–Hilliard equation, IEEE Trans. Image Process. 16 (2007) 285–291.
[13] I.C. Dolcetta, S.F. Vita, R. March, Area-preserving curve shortening flows: From phase separation to image processing, Interface Free Bound. 4 (2002) 325–434.
[14] Y. Li, J. Wang, B. Lu, D. Jeong, J. Kim, Multicomponent volume reconstruction from slice data using a modified multicomponent Cahn–Hilliard system, Pattern Recognit. 93 (2019) 124–133.
[15] Y. Li, J. Shin, Y. Choi, J. Kim, Three-dimensional volume reconstruction from slice data using a phase-field model, Comput. Vis. Image Und. 137 (2015) 115–124.
[16] M. Dehghan, V. Mohammadi, Comparison between two meshless methods based on collocation technique for the numerical solution of four-species tumor growth model, Commun. Nonlinear Sci. Numer. Simul. 44 (2017) 204–219.
[17] S.M. Wise, J.S. Lowengrub, H.B. Frieboes, V. Cristini, Three-dimensional multispecies nonlinear tumor growth - I: Model and numerical method, J. Theoret. Biol. 253 (2008) 524–543.
[18] V. Cristini, X. Li, J.S. Lowengrub, S.M. Wise, Nonlinear simulations of solid tumor growth using a mixture model: invasion and branching, J. Math. Biol. 58 (2009) 723–763.
[19] E. Kuhl, D.W. Schmid, Computational modeling of mineral unmixing and growth, Comput. Mech. 39 (2007) 439–451.
[20] J. Kim, A generalized continuous surface tension force formulation for phase-field models for multi-component immiscible fluid flows, Comput. Methods Appl. Mech. Engrg. 198 (2009) 3105–3112.
[21] L. Wang, H. Yu, An energy stable linear diffusive crank–nicolson scheme for the Cahn–Hilliard gradient flow, J. Comput. Appl. Math. 377 (2020) 112880.
[22] J. Guo, C. Wang, S.M. Wise, X. Yue, An improved error analysis for a second-order numerical scheme for the Cahn–Hilliard equation, J. Comput. Appl. Math. 388 (2021) 113300.
[23] J.S. Kim, J. Lowengrub, Phase field modeling and simulation of three-phase flows, Interfaces. Free Bound. 7 (2005) 435–466.
[24] M.I.M. Copetti, Numerical experiments of phase separation in ternary mixtures, Math. Comput. Simulation 52 (2000) 41–51.
[25] S. Bhattacharyya, T.A. Abinandanan, A study of phase separation in ternary alloys, Bull. Mater. Sci. 26 (2003) 193–197.
[26] H.G. Lee, J. Kim, A second-order accurate non-linear difference scheme for the N-component Cahn–Hilliard system, Physica A 387 (2008) 4787–4799.
[27] H.G. Lee, J.-W. Choi, J. Kim, A practically unconditionally gradient stable scheme for the N-component Cahn–Hilliard system, Physica A 391 (2012) 1009–01019.
[28] S. Wise, J.S. Kim, J. Lowengrub, Solving the regularized, strongly anisotropic Cahn–Hilliard equation by an adaptive nonlinear multigrid method, J. Comput. Phys. 226 (2007) 414–446.
[29] J. Yang, Y. Li, C. Lee, D. Jeong, J. Kim, A conservative finite difference scheme for the N-component Cahn–Hilliard system on curved surfaces in 3D, J. Eng. Math. 119 (2019) 149–166.
[30] Y. Li, H.G. Lee, B. Xia, J. Kim, A compact fourth-order finite difference scheme for the three-dimensional Cahn–Hilliard equation, Comput. Phys. Comm. 200 (2016) 108–116.
[31] J. Zhao, H. Li, Q. Wang, X. Yang, Decoupled energy stable schemes for a phase field model of three-phase incompressible viscous fluid flow, J. Sci. Comput. 70 (2017) 1367–1389.
[32] X. Yang, J. Zhao, Efficient linear schemes for the nonlocal Cahn–Hilliard equation of phase field models, Comput. Phys. Comm. 235 (2019) 234–245.
[33] Y. Li, J. Kim, N. Wang, An unconditionally energy-stable second-order time-accurte scheme for the Cahn–Hilliard equation on surfaces, Commun. Nonlinear Sci. Numer. Simul. 53 (2017) 213–227.
[34] Y. Li, X. Qi, J. Kim, Direct discretization method for the Cahn–Hilliard equation on an evolving surface, J. Sci. Comput. 77 (2) (2018) 1147–1163.
[35] Y. Li, C. Luo, B. Xia, J. Kim, An efficient linear second order unconditionally stable direct discretization method for the phase-field crystal equation on surfaces, Appl. Math. Model. 67 (2019) 477–490.
[36] M. Sun, X. Feng, K. Wang, Numerical simulation of binary fluid–surfactant phase field model coupled with geometric curvature on the curved surface, Comput. Methods Appl. Mech. Engrg. 367 (2020) 113123.
[37] M.A. Olshanskii, X. Xu, A trace finite element method for PDEs on evolving surfaces, SIAM J. Sci. Comput. 39 (2017) 1301–1319.
[38] C. Lehrenfeld, M.A. Olshanskii, X. Xu, A stabilized trace finite element method for partial differential equations on evolving surfaces, SIAM J. Numer. Anal. 56 (2018) 1643–1672.
[39] M. Dehghan, On the solution of an initial–boundary value problem that combines Neumann and integral condition for the wave equation, Numer. Methods Partial Differential Equations 21 (1) (2005) 24–40.
[40] M. Dehghan, M. Abbaszadeh, The space-splitting idea combined with local radial basis function meshless approach to simulate conservation laws equations, Alexandria Eng. J. 57 (2) (2018) 1137–1156.
[41] J.J. Hoyt, The continuum theory of nucleation in multicomponent systems, Acta Metall. 38 (1990) 1405–1412.
[42] Y. Li, J.-I. Choi, J. Kim, Multi-component Cahn–Hilliard system with different boundary conditions in complex domains, J. Comput. Phys. 323 (2016) 1–16.
[43] S.-G. Chen, J.-Y. Wu, Discrete conservation laws on curved surfaces II: A dual approach, SIAM J. Sci. Comput. 36 (4) (2014) 1813–1830.
[44] S.-G. Chen, J.-Y. Wu, Discrete conservation laws on curved surfaces, SIAM J. Sci. Comput. 36 (2) (2013) 719–739.
[45] D.J. Eyre, An Unconditionally Stable One-step Scheme for Gradient Systems, 1998. Unpublished article.
[46] Y. Li, J. Kim, An efficient and stable compact fourth-order finite difference scheme for the phase field crystal equation, Comput. Methods Appl. Mech. Engrg. 319 (2017) 194–216.
[47] B. Xia, C. Mei, Q. Yu, Y. Li, A second order unconditionally stable scheme for the modified phase field crystal model with elastic interaction and stochastic noise effect, Comput. Methods Appl. Mech. Engrg. 363 (2020) 112795.
[48] P. Yue, C. Zhou, J. Feng, Spontaneous shrinkage of drops and mass conservation in phase-field simulations, J. Comput. Phys. 223 (2007) 1–9.
[49] P.O. Persson, G. Stangt, A simple mesh generator in MATLAB, SIAM Rev. Soc. Ind. Appl. Math. 46 (2004) 329–345.
[50] F. Sun, Y.-K. Choi, W. Wang, D.-M. Yan, Y. Liu, B. Lévy, Obtuse triangle suppression in anisotropic meshes, Comput. Aided Geom. Design 28 (2011) 537–548.
[51] Y. Li, A. Yun, J. Kim, An immersed boundary method for simulating a single axisymmetric cell growth and division, J. Math. Biol. 65 (2012) 653–675.
[52] C. Talischi, G.H. Paulino, A. Pereira, I. F. M, Menezes PolyMesher: A general-purpose mesh generator for polygonal elements written in Matlab, Struct. Multidiscip. Optim. 45 (3) (2012) 309–328.
[53] Y. Li, A. Yun, D. Lee, J. Shin, D. Jeong, J. Kim, Three-dimensional volume-conserving immersed boundary model for two-phase fluid flows, Comput. Methods. Appl. Mech. Eng. 257 (2013) 36–46.